



Surface oxygenation induced strong interaction between Pd catalyst and functional support for zinc-air batteries

Journal:	<i>Energy & Environmental Science</i>
Manuscript ID	EE-ART-12-2021-003972.R1
Article Type:	Paper
Date Submitted by the Author:	10-Feb-2022
Complete List of Authors:	<p>Zhang, Wei; University of Central Florida, NanoScience Technology Center</p> <p>Chang, Jinfa; University of Central Florida, NanoScience Technology Center; University of Central Florida</p> <p>Wang, Guanzhi; University of Central Florida, NanoScience Technology Center</p> <p>Li, Zhao; University of Central Florida, NanoScience Technology Center</p> <p>Wang, Maoyu; Oregon State University, Chemical, Biological, and Environmental Engineering</p> <p>Zhu, Yuanmin; Southern University of Science and Technology</p> <p>Li, Boyang ; Univeristy of Pittsburgh, Mechanical Engineering and Materials Science</p> <p>Zhou, Hua; Argonne National Lab, Advanced Photon Source</p> <p>Wang, Guofeng; University of Pittsburgh, Mechanical Engineering and Materials Science</p> <p>Gu, Meng; Southern University of Science and Technology, MSE</p> <p>Feng, Zhenxing; Oregon State University, School of Chemical, Biological, and Environmental Engineering;</p> <p>Yang, Yang; University of Central Florida, NanoScience Technology Center</p>

Broader Context

Employing strong metal-support interaction (SMSI) effect for promoting the catalyst's activity toward oxygen reduction reaction (ORR) is promising due to electronic structure optimization and high utilization efficiency of platinum group metals (PGM) catalysts. We proposed a new strategy to strengthen the SMSI effects in a rationally designed materials system consisting of trace amount Pd embedded inside functionally oxygenated supports (FOS). We proved the significant role of FOS in regulating the electronic structure of Pd active sites and optimizing the adsorption and cleavage of O₂ during ORR. We also verified the role of FOS in serving as active phase for oxygen evolution reaction (OER), which make the proposed materials bifunctional for Zn-air batteries (ZAB). The proposed concept of FOS can be applied to broader fields where the SMSI plays a crucial role in realizing performance improvement.

Surface oxygenation induced strong interaction between Pd catalyst and functional support for zinc-air batteries

Wei Zhang^{1,2}, Jinfu Chang¹, Guanzhi Wang^{1,2}, Zhao Li^{1,2}, Maoyu Wang³, Yuanmin Zhu^{4,5}, Boyang Li⁶, Hua Zhou⁷, Guofeng Wang⁶, Meng Gu⁴, Zhenxing Feng^{3}, and Yang Yang^{1,2,8,9*}*

1. NanoScience Technology Center, University of Central Florida, Orlando, FL 32826, USA.
Email: Yang.Yang@ucf.edu
2. Department of Materials Science and Engineering, University of Central Florida, Orlando, FL 32826, USA.
3. School of Chemical, Biological, and Environmental Engineering, Oregon State University, Corvallis, OR 97331, USA. E-mail: zhenxing.feng@oregonstate.edu
4. Department of Materials Science and Engineering, Southern University of Science and Technology, Shenzhen 518055, China.
5. Department of Materials Science and Engineering, Dongguan University of Technology, Dongguan 523808, China
6. Department of Mechanical Engineering and Materials Science, University of Pittsburgh, Pittsburgh, PA 15261, USA.
7. X-ray Science Division, Argonne National Laboratory, Lemont, IL 60439, USA
8. Renewable Energy and Chemical Transformation Cluster, University of Central Florida, Orlando, FL 32826, USA.
9. Department of Chemistry, University of Central Florida, Orlando, FL 32826, USA.

Abstract

Employing strong metal-support interaction (SMSI) effect for promoting the catalyst's activity toward oxygen reduction reaction (ORR) is promising due to electronic structure optimization and high utilization efficiency of platinum group metals (PGMs) catalysts. Metal oxides as alternative supports for PGM facilitate intrinsic activity and improve durability compared to conventional carbon supports. However, the restricted mass and electron transfer at the metal/support interface need to be addressed. Herein, to strengthen the interaction at the metal/support interfaces and improve the utilization efficiency of PGM, ultralow loading of Pd was embedded in a surface-oxygenated PdNiMnO porous film. The Mn-doping was designed to promote surface oxygenation using a facile anodization process that created sufficiently exposed interfaces between Pd and support, strengthening the SMSI effects at the Pd/oxygenated support interface for enhancing ORR performance. Furthermore, the Ni-containing oxygenated catalyst served as both the active component for oxygen evolution reaction (OER) and functional support for stabilizing Pd, making PdNiMnO a bifunctional catalyst for zinc-air flow batteries (ZAFB). As a proof-of-concept, the ZAFB (PdNiMnO) shows a maximal power density of $211.6 \text{ mW} \cdot \text{cm}^{-2}$ and outstanding cycling stability for over 2000 h with a minimal voltage gap of 0.69 V at a current density of $10 \text{ mA} \cdot \text{cm}^{-2}$, superior to the state-of-the-art catalysts.

Keywords: catalyst-support interaction; Pd; functional support; oxygenated surface; zinc-air batteries

Introduction

Nowadays, growing markets for consumer electronics and electrical cars spur the development of energy conversion and storage technologies with high efficiency and sustainability.^{1,2} So far, enormous efforts and investments have been focused on the emerging Zn-air batteries (ZAB) due to their superior theoretical energy density compared to Li-ion batteries (LIB).^{3,4} In addition, low cost, zero-emission, and less toxic aqueous electrolytes largely reduce safety and environmental concerns.³ The discharging performance of ZAB is markedly dependent on oxygen reduction reaction (ORR) at the cathode, during which O₂ receives electrons and is reduced to the hydroxyl group in an alkaline environment, and vice versa for oxygen evolution reaction (OER), shaping the charging behavior. However, the performance of ZAB is significantly inhibited by the sluggish 4-electron transfer process and large overpotentials at the cathode caused by the barriers for surface electrochemical processes on the catalysts including O₂ adsorption/desorption, O-O cleavage/association as well as interaction with oxygen-containing intermediates.^{5,6} Thus, developing a highly efficient bifunctional catalyst for the cathode reaction is of vital importance. It is widely accepted that platinum group metals (PGMs) are essentially the most efficient catalysts for ORR/OER compared to the transition metals due to their unique electronic structures interacting with oxygen molecules and intermediate species.^{7,8} Nevertheless, the high cost of PGM-based catalysts significantly hinders the rapid growth of the ZAB market in the field of renewable energy.

To overcome the cost barrier, extensive efforts have been devoted to the exploration of various strategies to improve the performance of low-PGM and non-PGM catalysts in order to pursue the increasing demands for highly efficient energy storage and conversion systems. For instance, surface/interface engineering has been demonstrated to be an efficient strategy for

tuning the size, shape, and surface morphology of the catalysts to accommodate less PGM at the interfaces.⁹ Alloying PGM with transition metals (Fe, Co, Ni) can sufficiently expose the active sites and modify the electronic structures of PGM.¹⁰⁻¹² Engineering the interface between metal and oxides can promote interfacial electron/mass (O_2 , intermediate species, and products) transfer.^{13, 14} In addition, transition metal oxides (e.g., MnO_x , CoO_x , FeO_x) with multiple chemical states may show unique adsorption/interaction with oxygen, however, which are still inferior to the PGM-based ORR catalysts due to the poor electron transfer across the interfaces.^{15, 16} Besides, employing strong metal-support interaction (SMSI) is a promising way for tuning electronic structure at the materials interfaces, which is responsible for the preeminent catalytic activities.^{17, 18} For example, improved ORR activities were achieved on Pt/ NbO_x interfaces in the Pt/ NbO_x /C system by shortening Pt-Pt bond distance and constructing electron-deficient low-coordination Pt sites.¹⁷ Whereas a reverse trend was observed for electron donation from NbO_2 layer to Pt layer, leading to excessive electrons on Pt that tuned the interaction between chemisorbed species and Pt sites.¹⁹ Thus, the degree of oxygen incorporation, morphology as well as electronic structure at the metal/support interface together determine the SMSI effect and thus the ORR performance. However, most of the oxide supports (e.g., NbO_x) designed for SMSI are inert to both ORR and OER, thus limiting their practical applications in ZAB. Therefore, we suggest that functionally oxygenated supports (FOS) with maximal exposure area of PGM and active components for OER will be an ideal option for applying the SMSI effect in ZAB, which ensure the improved electron and mass transfer across the interfaces.

When applying the SMSI effect in designing novel PGM-based catalysts, the FOS possesses many advantages over conventional supports because of their ability to modulate the electronic structure of active sites, which further optimize the adsorption and cleavage of O_2 .²⁰ In addition,

compared with PGM alloy and traditional carbon-based PGM, which may undergo severe PGM dissolution, agglomeration, and Ostwald ripening, etc. during the long period of operation due to leaching of transition group metal and carbon corrosion²¹, the preeminent features of carbon-free FOS for preventing PGM from deactivation based on strong SMSI effect during the operation of ZAB make them promising candidates to replace conventional supports.^{22, 23} Furthermore, the FOS can serve as secondary adsorption sites for reaction intermediates, which play a crucial role in lowering the reaction energy barrier.^{22, 24} However, the traditional synthesis routes (e.g., high-temperature annealing and vacuum deposition) of FOS can only produce a limited number of catalyst/support interfaces,^{18, 25} which severely lowers the surface active sites and thus hinders the mass transfer process.^{17, 26} Besides, the poor electron transfer across the interfaces obstructs the delivery of the intrinsic catalytic activity in ZAB.²⁷ Thus, it is non-trivial to develop an efficient approach to FOS with sufficiently exposed catalyst/support interfaces for favoring mass and electron transfer by virtue of the SMSI effect.

Pd-based catalysts are promising alternatives to Pt-based materials for ORR due to their similar catalytic activity but higher abundance than Pt.²⁸⁻³⁰ However, modulating the electronic structure of Pd to optimize surface reaction kinetics towards ORR is still required.³¹ To this end, we suggest building up a porous film (PF) of the Pd/FOS catalyst with a rationally designed oxygenated support for the boosted SMSI effect. The porous structure of Pd/FOS can effectively expose active sites on the surface and strengthen the interaction between Pd and FOS, thus ensuring high activity throughout the porous network. Our prior studies prove that the anodization treatment is a facile approach to the surface oxygenated Ni-based porous materials for electrocatalytic reactions,³² which was adopted in this work for the synthesis of the proposed Pd/FOS-PF, as Pd could be embedded in the oxygenated Ni support (FOS). We also doped Mn into Ni-based PF to

promote the formation of surface oxygenation and tune the valence state of metals because of the various oxidation states of Mn^{x+} ($x = 2, 3, 4, 6, 7$).³³ Furthermore, the surface oxygenated Mn-doped Ni porous film (denoted as NiMnO-PF, which represents general chemical composition instead of exact stoichiometry) can serve as FOS for the immobilization of Pd catalysts as well as an active component for OER in ZAB. The novel surface oxygenation strategy ensures the seamless interaction between countless Pd/FOS interfaces compared with the conventional metal-support system. This strengthened SMSI effect will benefit the mass and electron transfer as well as stabilize the exposed Pd active sites for long-term utilization in ZAB.^{20, 34}

Herein, to verify the aforementioned concept of Pd/FOS-PF in promoting ZAB performance throughout the SMSI effect, we electrodeposited PdNiMn film with ultralow Pd loading as precursor materials, which were then anodized to form oxygenated PdNiMnO-PF. As a result, the oxygenation of Ni and Pd was achieved in the PdNiMnO-PF than the control catalyst of PdNiO-PF without Mn because of the promoted surface oxygenation by Mn-doping. Note that “PdNiMnO” represents metallic Pd, PdO as well as FOS instead of exact stoichiometry. Therefore, the strengthened interaction between Pd and oxygenated NiMnO-PF support is responsible for the boosted ORR activity due to the accelerated charge transfer across the Pd/NiMnO interfaces. Also, the formed oxygenated phase around Pd active sites may act as secondary adsorption sites for lowering the reaction energy barrier.^{24, 35} On the other hand, the NiMnO is the active component for OER, enabling the PdNiMnO-PF bifunctional ORR/OER activities for ZAB applications.^{36, 37} As a proof-of-concept, Zn-air flow batteries (ZAFB) assembled with PdNiMnO-PF as the cathode delivered a maximum power density of $211.6 \text{ mW} \cdot \text{cm}^{-2}$ and ultrahigh cycling stability for 2000 h, superior to state-of-the-art catalysts.

Results and Discussion

A bottom-up electrodeposition method (see supporting information for experimental details) was employed to synthesize the PdNiMn film, followed by a top-down anodization treatment to fabricate PdNiMnO-PF consisting of well-pronounced surface oxygenation of metals. The porous structure of PdNiMnO-PF showing an interconnected network not only enables the easy access of electrolyte towards Pd/NiMnO for the electrocatalysis of O₂ but also facilitates the electron transfer across the Pd/NiMnO interface due to the strong SMSI effect. Scanning electron microscope (SEM) images (**Figure 1a-c**) display an interconnected porous structure of PdNiMnO-PF with pore size in a range of 30-100 nm. We also prepared PdNiO porous film (denoted as PdNiO-PF) as a control catalyst to study the role of Mn in forming surface oxygenation (**Figure S1**). The exposed electrochemical active surface area (ECSA) of PdNiMnO-PF and PdNiO-PF for electrochemical reactions were estimated by calculating the electrical double layer capacitance (C_{dl} , **Figure S2**), similar to C_{dl} measured from electrochemical impedance spectroscopy (EIS) at open circuit potential (OCP)³⁸ (**Figure S3**). Note that the non-rectangular shape of CV curves is attributed to non-ideal capacitor behavior due to non-uniform pore structure and current distribution.³⁹ The PdNiMnO-PF has a higher ECSA than PdNiO-PF, opening more active surface sites for the catalytic reactions.

High-resolution transmission electron microscopy and high-angle annular dark-field scanning transmission electron microscopy (HAADF-STEM) images (**Figure 1d-f**) show the porous and well-crystallized structure of PdNiMnO-PF, suggesting the presence of a large number of small boundaries between Pd and NiMnO, which ensures a large amount of exposed Pd/NiMnO interfaces thus can maintain the intimate electron transfer across the interfaces between Pd and oxygenated support. The d-spacings of 0.24 nm and 0.26 nm were identified, corresponding to the lattice planes of NiO (111)⁴⁰ and PdO (101),⁴¹ respectively, confirming the coexistence of the

surface oxygenated metals. Also, the metallic Pd active sites with a d-spacing of 0.22 nm, corresponding to the Pd (111) plane, were identified around the neighboring oxygenated phase. HAADF image (**Figure 1g**) and corresponding energy-dispersive X-ray spectroscopy (EDS) for elemental mapping (**Figure 1h-l**) of PdNiMnO-PF show the distribution of Pd, Ni, Mn, and O over the porous structure. The circled area (untreated region underneath the catalyst layer) dominantly consists of Ni and other minor elements. On the contrary, the distribution of Pd, Ni, Mn, and O outside the circled area is highly matched, suggesting that the surface oxygenation is promoted probably due to the improved lattice oxygen diffusion induced by the incorporation of multivalence Mn.^{33, 42} Moreover, the cross-sectional HAADF image (**Figure S4a**) and corresponding EDS elemental mapping (**Figure S4b-f**) of PdNiMnO-PF show the overall element distributions across the catalyst. An apparent phase boundary between the catalyst layer (PdNiMnO-PF) and compact PdNiMn substrate (untreated region and used as conducting current collector in ZAB) was observed. The increased relative concentration of Pd in the surface porous structure of the catalyst layer implies the sufficiently exposed Pd active sites and morphology reconstruction by anodization. Note that the PdNiMnO-PF directly grew on the underneath PdNiMn substrate, forming a seamless interface that ensures high conductivity throughout the catalyst. The electron microscopy characterizations prove the successful fabrication of PdNiMnO-PF via one-pot electrodeposition coupled with a top-down anodization process.

To further probe the structural characteristics of the catalysts, X-ray diffraction (XRD, **Figure S5**) was employed to study the phase compositions of PdNiMnO-PF and PdNiO-PF. The PdNiMn substrate underneath the porous films of PdNiMnO-PF and PdNiO-PF were identified at 44.5°, 51.9°, and 76.5°, corresponding to Ni (111), (200), and (220), respectively (JCPDS: 1-1258). Note that the peak of oxygenated Ni and Mn is absent in the diffraction pattern of PdNiMnO-PF because

of the low content of the catalyst layer formed on the top surface of the materials, so does the PdNiO-PF. X-ray fluorescence was used to quantify the bulk elemental information across the whole film. The atomic contents of Ni, Pd, and Mn are 99.25 at%, 0.41 at%, and 0.33 at%, respectively, for the PdNiMnO-PF, which are similar to those for the PdNiO-PF (**Table S1**). Moreover, an ultralow loading of Pd in the PdNiMnO-PF was calculated to be 0.016 ± 0.008 mg·cm⁻² (**Table S2**), remarkably reducing the cost of the catalysts used in the energy devices.

X-ray photoelectron spectroscopy (XPS) was utilized to acquire the surface chemical states of PdNiMnO-PF and PdNiO-PF. The XPS Ni 2p spectra (**Figure 2a**) show the presence of Ni⁰ (852.8 and 870.2 eV) and oxygenated Ni (855.9 and 873.9 eV) for PdNiMnO-PF, and Ni⁰ (852.6 and 870.0 eV), as well as oxygenated Ni (855.8 and 873.8 eV) for PdNiO-PF, the positive binding energy (BE) shift of ~0.1 eV for oxygenated Ni in PdNiMnO compared to PdNiO, indicates the electron-donating nature of oxygenated support.^{43, 44} Moreover, XPS O 1s spectra (**Figure 2b**) show lattice oxygen (M-O) peak at the BE of 529.9 eV for PdNiMnO-PF, which is negatively shifted by ~0.22 eV for PdNiO-PF (529.7 eV), implying the regulated electron-donating ability of lattice oxygen by Mn-doping as well. The BE of 531.7 and 533.4 eV for both PdNiMnO-PF and PdNiO-PF are attributed to the hydroxyl groups and water, respectively.⁴⁴ And these hydroxyl groups may promote the desorption/removal of oxygen-containing intermediates, facilitating the reaction kinetics.^{20, 30} More importantly, a negative BE shift of ~0.32 eV for Pd⁰ (**Figure 2c**) was identified in the PdNiMnO-PF (335.1 and 340.4 eV) compared with PdNiO-PF (335.4 and 340.7 eV), indicating the modified electron-withdrawing ability of Pd⁰ by forming oxygenated surface. Also, the BE assigning to Pd²⁺ is negatively shifted in the PdNiMnO-PF (335.8 and 341 eV) compared to PdNiO-PF (336.3 and 341.6 eV), suggesting the electron redistribution at the Pd/support interface.⁴⁵ It is also noteworthy that a higher concentration of Pd²⁺ was detected in the

PdNiMnO-PF (39.4%) than PdNiO-PF (16.7%), confirming the promoted formation of the oxygenated catalyst surface by Mn-doping. The notable electron transfer from oxygenated catalyst surface to Pd observed in the PdNiMnO-PF indicates the tailored electronic structure at the Pd/support interface,^{17, 46} which may facilitate the reaction kinetics and O-O bond cleavage.³⁰ Based on the XPS characterization and analysis, the oxygenated catalyst around Pd may behave as secondary adsorption sites for oxygen-containing intermediates (e.g., *OOH, *OH, and *O), thus lowering the reaction barrier.^{24, 35} However, we could not detect Mn 2p XPS signal due to the overlapped binding energy range with Ni LMM Auger peak (**Figure S6**),⁴⁷ suggesting the low doping content of Mn.³³ Ultraviolet photoelectron spectroscopy (UPS, **Figure S7**) was used to estimate the work function (WF) of the catalysts. A smaller WF of PdNiMnO-PF (4.7 eV) was obtained than that of PdNiO-PF (5.24 eV), indicating the higher mobility and less hurdle for electrons to participate in the surface reactions.^{48, 49} Meanwhile, Raman spectroscopy (**Figure 2d**) was employed to probe the oxygenated phase and identify the degree of surface oxygenation. A Raman peak centered at 508 cm⁻¹ assigning to the Ni-O stretching vibration mode was observed in both PdNiMnO-PF and PdNiO-PF, further confirming the formation of oxygenated Ni in the porous films.⁵⁰ Compared with PdNiO-PF, the PdNiMnO-PF displays more pronounced Pd-O vibration modes of E_g (431 cm⁻¹) and B_{1g} (634 cm⁻¹), indicating the higher amount of surface oxygenated Pd formed in the PdNiMnO-PF than PdNiO-PF. While other weaker lines located at 273 cm⁻¹ and 330 cm⁻¹ are assigned to resonance/secondary scattering effect.⁴⁵ In all, the spectroscopic analyses are consistent with TEM results, confirming the strengthened SMSI effect for surface catalysis.

To further understand the Pd, Ni, and Mn interaction in the PdNiMn-PF, X-ray absorption spectroscopy (XAS) was carried out to probe the electronic state and atomic local structure.^{48, 51,}

⁵² X-ray absorption near edge structure (XANES) of PdNiMn film indicates all three metals (Pd, Ni, and Mn) stay in the metallic form (**Figure S8**). However, there are some differences between metallic states in reference samples and alloy states, indicating some interactions between Pd, Ni, and Mn, which could be due to the formation of Pd-Ni/Mn bonds and then result in electron transfer between Pd, Ni, and Mn to promote the reaction kinetics. The extended X-ray absorption fine structure (EXAFS) further confirms those interactions (**Figure 3**). Comparing metallic Pd with Pd in PdNi and PdNiMn in Fourier-transformed EXAFS (**Figure 3a**), the locations of the first peak (2.2 Å) of PdNi and PdNiMn is lower than that of the metallic bonding Pd-Pd peaking (2.5 Å), which means that Pd forms a new shorter bonding with Ni. The 2D wavelet transform of Pd K-edge also confirms that Pd creates new bonding with Ni due to the new peak formation around 7Å^{-1} (**Figure 3b** and **Figure S9**) that does not present in the metallic Pd. After the Mn adding, the first peak around 2.2 Å in Mn K-edge is also smaller than the metallic Mn-Mn peak around 2.4 Å (**Figure 3a**), which can be attributed to the shorter Mn-Ni bonds. It is hard to see the difference in Ni K-edge and Pd K-edge due to the addition of a small amount of Mn. However, when carefully checking the wavelet transform of Mn K-edge between PdNiMn and metallic Mn, the second peak at around 8.6Å^{-1} in PdNiMn is broader than the one shown in metallic Mn (**Figure 3b** and **Figure S9**). The peak intensity and shape of both Ni K-edge and Pd K-edge in PdNiMn and PdNi changes, suggesting that Mn interacts with both Ni and Pd to form new bonds. Therefore, the XAS results verify that Mn is bonded with both Pd and Ni in PdNiMn, which is consistent with TEM analyses and could be the reason to promote the surface oxygenation in the catalysts.

The well-constructed 3D porous structure of PdNiMnO-PF synthesized by anodization benefits the Pd-support interaction for surface catalysis and ensures the intimate contact between catalysts and electrolytes (**Figure 4a**). The electron-rich characteristic of Pd is responsible for the

promoted O-O cleavage and facilitated ORR reaction kinetics.^{17, 53} The electrocatalytic ORR performance of the catalysts was evaluated using a three-electrode cell in 0.1 M KOH with a rotating ring disk electrode (RRDE) as the working electrode to study the intrinsic electron transfer number (n) and hydrogen peroxide yield ($\chi_{\text{H}_2\text{O}_2}$ (%)) for ORR. All voltages mentioned below are referred to as reversible hydrogen electrode (RHE). A set of cathodic peaks located at 0.82 and 0.70 V was observed in the cyclic voltammetry (CV) curves recorded in O₂-saturated electrolyte for PdNiMnO-PF, corresponding to O₂ and Pd-O reduction peaks, respectively (**Figure 4b**).⁵⁴ Whereas only the Pd-O reduction peak (0.70 V) was observed in the N₂-saturated electrolyte, confirming an apparent Pd-O reduction and surface oxygenation on the catalyst. Note that the current density of Pd-O reduction peak in CV curves for PdNiMnO-PF is significantly higher than that for PdNiO-PF and PdNiMn metal porous film (PdNiMn-MPF, **Figure S10**). This further confirms the presence of the oxygenated Pd in PdNiMnO-PF with a higher degree of surface oxygenation. Note that we compared PdNiMnO-PF with PdNiMn-MPF in order to verify the efficacy of the SMSI effect.

Linear sweep voltammetry (LSV) was conducted at 1600 rpm to further explore the ORR performance and electron transfer pathways of the catalysts. The n and $\chi_{\text{H}_2\text{O}_2}$ (%) of PdNiMnO-PF and other control catalysts measured at 0.4 V are summarized in **Figure 4c**. It is noticed that the PdNiMnO-PF (**Figure S11a**) shows a negligible H₂O₂ yield (5.6%) and an enhanced electron transfer kinetics ($n = 3.89$, **Figure S11b**), which are much better than the control samples (PdNiMn film, PdNiMn-MPF, and PdNiO-PF) and comparable to Pd/C catalyst. This implies that the surface oxygenation and porous structure improved the electron transfer towards the complete 4-electron pathway and significantly suppressed the H₂O₂ production.^{24, 35} The LSV curves (**Figure S12**) were further analyzed to evaluate the ORR activities of the catalysts by checking the onset potential

when current density exceeds $0.1 \text{ mA}\cdot\text{cm}^{-2}$ (E_{onset}), half-wave potential ($E_{1/2}$), and diffusion-limiting current (J_d), which are summarized in **Figure 4d**. The PdNiMnO-PF shows more positive E_{onset} of 0.94 V and $E_{1/2}$ of 0.84 V than PdNiO-PF and PdNiMn-MPF, and comparable to Pd/C. Also, the PdNiMnO-PF exhibits a higher J_d of $6.3 \text{ mA}\cdot\text{cm}^{-2}$ than PdNiMn-MPF ($5.2 \text{ mA}\cdot\text{cm}^{-2}$), PdNiO-PF ($6.2 \text{ mA}\cdot\text{cm}^{-2}$), and Pd/C ($5.7 \text{ mA}\cdot\text{cm}^{-2}$), which is very close to the theoretical value of J_d of $6 \text{ mA}\cdot\text{cm}^{-2}$ at a rotating speed of 1600 rpm and the higher value is ascribed to the porous structure.⁵⁵ The overall ORR performance of PdNiMnO-PF is superior to the control catalysts, convincing the merits of the enhanced Pd-support interaction. Besides, to further verify the significance of surface oxygenation in promoting ORR performance, we prepared PdNiMnO-PF with different oxygenation degrees by tuning the H₂O content added to the anodization electrolytes. The catalysts show slightly different ORR performance (**Figure S13**) by varying the oxygenation degrees with the PdNiMnO-PF (2M) sample showing the optimal ORR performance (**Table S3**) and highest Pd-O reduction area, which confirms the relation between surface oxygenation and ORR performance. In addition, the PdNiMnO-PF shows a much higher specific activity (SA) of $253 \mu\text{A}\cdot\text{cm}^{-2}_{\text{Pd}}$ than those of Pd/C ($233 \mu\text{A}\cdot\text{cm}^{-2}_{\text{Pd}}$), PdNiO-PF ($160 \mu\text{A}\cdot\text{cm}^{-2}_{\text{Pd}}$), and PdNiMn-MPF ($90 \mu\text{A}\cdot\text{cm}^{-2}_{\text{Pd}}$, **Figure 4e**), indicating the greatly improved utilization efficiency of Pd embedded in the porous structure. The PdNiMnO-PF also delivers a remarkably larger mass activity (MA) of $180.9 \text{ A}\cdot\text{g}^{-1}_{\text{Pd}}$ than those of Pd/C ($163.6 \text{ A}\cdot\text{g}^{-1}_{\text{Pd}}$), PdNiO-PF ($48.4 \text{ A}\cdot\text{g}^{-1}_{\text{Pd}}$), and PdNiMn-MPF ($39.7 \text{ A}\cdot\text{g}^{-1}_{\text{Pd}}$). Furthermore, the PdNiMnO-PF shows a higher EASA_{Pd} of $81.9 \text{ m}^2\cdot\text{g}^{-1}_{\text{Pd}}$ than those of Pd/C ($68.7 \text{ m}^2\cdot\text{g}^{-1}_{\text{Pd}}$), PdNiO-PF ($26.6 \text{ m}^2\cdot\text{g}^{-1}_{\text{Pd}}$), and PdNiMn-MPF ($39.75 \text{ m}^2\cdot\text{g}^{-1}_{\text{Pd}}$), indicating the significantly increased accessible surface area of the catalysts to the electrolyte.⁵⁶ Chronoamperometry test (**Figure S14**) was performed to investigate the electrochemical stability of PdNiMnO-PF at 0.6 V in O₂-saturated 0.1 M KOH electrolyte, which

shows improved stability and higher current retention (83.6%) than Pd/C (71.3%) after 12 hours of stability test, due to the inhibited Pd deactivation in the oxygenated support.^{20, 30}

We performed the first-principles density functional theory (DFT) calculations to gain insight into the role of Mn in affecting the activity and durability of the PdNiMnO-PF catalyst. Our calculations predicted that Mn was energetically more favorable to be doped in the sublayer than the outermost layer of Pd(111) surface (as shown in **Figure S15** and denoted as Mn-Pd(111)). **Figure S16** shows that the free energy changes for all the elementary steps of ORR on Mn-Pd(111) become negative under an electrode potential of 0.71 V, higher than that of 0.68 V for ORR on undoped Pd(111). This result indicates that sublayer Mn weakens the interaction between Pd and ORR intermediates and thus enhances the ORR activity of Pd(111). Moreover, the enthalpy change for the demetallation of a Pd atom from the outermost layer of Mn-Pd(111) was predicted to be 4.71 eV, higher than that of 4.66 eV for that from undoped Pd(111), suggesting that the sublayer Mn could also stabilize the outermost surface Pd atoms (**Figure S17**). In conclusion, our DFT results reveal that subsurface Mn could enhance the ORR activity and stability of Pd catalysts, explaining well our experimental observations in **Figure 4**.

Furthermore, we conducted TEM, SEM, XRD, XPS, UPS, and Raman to verify the structural integrity of PdNiMnO-PF after the stability test. The structure and composition of the catalyst after the stability test (denoted as PdNiMnO-stability) are well consistent with the fresh catalyst, as proved by HRTEM and STEM-HAADF images (**Figure S18**) as well as EDS mappings (**Figure S19**). As confirmed by SEM images (**Figure S20**), the porous structure of PdNiMnO-PF was well maintained without collapse after the stability test. XRD (**Figure S5**) shows the intact structure of PdNiMnO-stability compared with the fresh catalyst. Moreover, XPS (**Figure S21**) and UPS (**Figure S22**) were employed to investigate the electronic structure of PdNiMnO-stability. The

XPS Ni 2p spectrum shows the presence of Ni²⁺ (855.8 and 873.6 eV) and largely decreased Ni⁰ (852.8 and 870.2 eV).⁵⁷ The XPS Pd 3d spectrum shows Pd⁰ (335.18 and 340.45 eV) and Pd²⁺ (335.96 and 341.23 eV), implying a negligible BE change compared to the fresh catalyst. Also, the XPS O 1s spectrum displays the BE of lattice oxygen at 529.86 eV, similar to the fresh catalyst.⁴⁴ Moreover, the WF of PdNiMnO-stability estimated by UPS is 4.76 eV, consistent with the fresh catalyst. Besides, Raman shift (**Figure S23**) of PdNiMnO-stability located at 273 cm⁻¹, 330 cm⁻¹, 431 cm⁻¹, and 634 cm⁻¹ are attributed to Pd-O. It is noteworthy that a new stretching vibration mode appears at around 555 cm⁻¹ except for the Ni-O at 508 cm⁻¹ compared to the fresh catalyst due to the formation of Ni(OH)₂,⁵⁸ which was also confirmed by the lattice fringe of 0.233 nm identified from HRTEM (**Figure S18**), corresponding to the plane of Ni(OH)₂ (101). This surface reconstruction on the oxygenated Ni could largely impede the detachment of Pd into the electrolyte due to circumvented Ni leaching and associated chemical/physical blockage of dissolution of Pd⁵⁹,⁶⁰. Moreover, the TEM-EDS and XPS elemental composition analysis demonstrated high consistency before and after the stability test (**Table S4**). Therefore, the strong metal-support interaction and surface reconstruction could synergistically stabilize Pd during the alternative ORR/OER process in an alkaline environment. The microscopic and spectroscopic characterizations confirmed the structural and electronic structure integrity of PdNiMnO-PF after the electrochemical stability test.

We further examine the OER activity of PdNiMnO-PF by checking LSV curves (**Figure S24**). A potential (@10 mA·cm⁻²) of 1.59 V is obtained for PdNiMnO-PF, same to PdNiO-PF (1.59 V) and superior to NiMnO-PF (1.65 V). Also, the significantly inferior OER performance of Pd/C compared to PdNiMnO-PF suggests that Pd has no activity towards OER, indicating that the NiMnO is the active phase for OER.³⁶ The superior OER performance of PdNiMnO-PF compared

to other control catalysts confirms the efficacy of Pd/FOS catalyst due to strong SMSI. Therefore, a rationally designed electrode can be achieved by utilizing Pd as ORR active site embedded in the NiMnO functional support (OER active phase) through SMSI in the porous network that can synergistically behave as a highly efficient bifunctional catalyst for ZAB.

Based on the superiority of overall potential difference between ORR($E_{1/2}$) and OER($E_{@10\text{ mA}\cdot\text{cm}^{-2}}$) for PdNiMnO-PF compared to other catalysts (**Figure S25**), rechargeable zinc-air flow batteries (ZAFB) were assembled using PdNiMnO-PF as the cathode catalysts and Zn plates as the anodes (**Figure 5a**). The OCP of ZAFB (PdNiMnO) was measured to be 1.37 V (V vs Zn/Zn²⁺ for zinc-air battery), higher than that of ZAFB (Pt/C-RuO₂) (1.35 V, **Figure S26**). A green LED lamp was lighted up by two ZAFBs (PdNiMnO) connected in series (**Figure S27**). A peak power density of 211.6 mW·cm⁻² at a current density of 377 mA·cm⁻² (**Figure 5b**) was achieved for ZAFB (PdNiMnO), surpassing that of ZAFB (Pt/C-RuO₂) (106.2 mW·cm⁻² at 234 mA·cm⁻²). Moreover, the ZAFB (PdNiMnO) delivered a specific capacity and energy density of 812.9 mAh·g⁻¹ and 958 Wh·kg⁻¹, respectively, superior to those of ZAFB (Pt/C-RuO₂) (779.1 mAh·g⁻¹ and 860.3 Wh·kg⁻¹, **Figure S28**). Besides, discharge curves at various current densities (5-50 mA·cm⁻²) are shown in **Figure 5c** to evaluate the rate capacity of ZAFB. The ZAFB (PdNiMnO) shows more prominent discharge capacities at high current densities (10-50 mA·cm⁻²) than ZAFB (Pt/C-RuO₂), proving the facilitated reaction kinetics enabled by the enhanced Pd-support interaction of PdNiMnO-PF. The voltage gap (ΔV) between charge/discharge potential difference during ZAFB operation and peak power density of ZAFB (PdNiMnO) were illustrated in the characteristic plot (**Figure 5d**) to compare with other state-of-the-art catalysts. The ZAFB (PdNiMnO) delivered an optimized performance regarding the voltage gap and power density (**Table S5**) among the state-of-the-art catalysts for ZAB, including PGM-based materials,^{11, 48, 57,}

⁶¹ transition metal-based materials,⁶²⁻⁶⁴ carbon-based composites,⁶⁵⁻⁷¹ and some emerging single-atom catalysts.⁷² The superior performance over state-of-the-art results from the seamless Pd/FOS interaction that contributes to the fast mass/electron transport, ensuring the stabilization of Pd in the FOS network.

To confirm the oxidation of Pd experienced during the charging process will not impact the activity and stability of the ZAFB, we performed XPS characterization on probing chemical state and composition of Pd right after the charging process of the last cycle (65 hours, 130 cycles) at a current density of $10 \text{ mA} \cdot \text{cm}^{-2}$. As expected, the Pd formed a more oxidized state (71.4%) after the charging process revealed from high-resolution XPS Pd 3d spectra (**Figure S29a**), in contrast to a more metallic state (66.7%) before charging (**Figure S29b**). However, this oxidation of Pd after charge will not affect the excellent performance of ZAFB in a long-term operation due to the metallic Pd will be reversibly formed during the discharging process, as confirmed by the reduced voltage gap read from **Figure S29c**. Furthermore, the stability of ZAFB (PdNiMnO) was tested by performing charging/discharging cycling at $10 \text{ mA} \cdot \text{cm}^{-2}$ (**Figure 5e**) for 2000 h (4000 cycles), which did not show any performance degradation. On the other hand, the voltage gap of 1 V (first 10 h cycles) gradually decreased to 0.69 V (last 10 h cycles, **Figure S30**), outperforming the ZAFB (Pt/C-RuO₂). This remarkable cycling stability of ZAFB (PdNiMnO) proves the merits of the SMSI effect in inhibiting Pd deactivation through strengthening the Pd-support interaction using oxygenated functional support^{17, 20, 34}, thus confirming the novelty of seamless interaction between countless Pd/FOS interfaces enabled by surface oxygenation strategy compared with other state-of-the-art catalysts. The proposed concept of coupling of low-PGMs with functional oxygenated support provides a new strategy for bifunctional catalyst design possessing countless and seamless interfaces.

Conclusion

In summary, we rationally designed and verified the SMSI effect by promoting surface oxygenation in the porous film via Mn-doping. The strengthened Pd-support interaction tailors the electronic structure of Pd active sites for ORR due to the strong coupling with neighboring oxygenated catalysts, redistributing the local electron density. As a result, the accelerated electron transfer and boosted reaction kinetics were achieved in the PdNiMnO-PF for ORR in addition to the secondary adsorption sites for the intermediates. Meanwhile, the oxygenated support also served as the active phase for OER, enabling the PdNiMnO-PF bifunctional abilities for ZAFB. As a proof-of-concept, the ZAFB (PdNiMnO) delivered significantly improved cyclability (over 2000 h, 4000 cycles) and peak power density of $211.6 \text{ mW}\cdot\text{cm}^{-2}$, as well as a greatly reduced voltage gap (0.69 V). The proposed concept of low-Pd/functionally oxygenated support interaction sheds a light on designing novel catalysts for various electrochemical energy applications.

Supporting Information

Supporting Information is available from the author.

Corresponding Author

Yang Yang - *NanoScience Technology Center, Department of Materials Science and Engineering, Renewable Energy and Chemical Transformation Cluster, Department of Chemistry, University of Central Florida, Orlando, FL 32826, USA. Email: Yang.Yang@ucf.edu*

Zhenxing Feng - *School of Chemical, Biological, and Environmental Engineering, Oregon State University, Corvallis, OR 97331, USA. E-mail: zhenxing.feng@oregonstate.edu*

Acknowledgements

Y.Y. thanks the support by the National Science Foundation under Grant No. CMMI-1851674, CBET-194984, and the startup grant from the University of Central Florida. The XPS

characterization was supported by the National Science Foundation NSF MRI: XPS: ECCS: 1726636, hosted in MCF-AMPAC facility, MSE, CECS, UCF. The Raman characterization was supported by the National Science Foundation under Grant No. DMR 1920050 (MRI). The XAS characterization (Z.F.) was supported by the National Science Foundation under Grant No. CBET-1949870. The use of the Advanced Photon Source at Argonne National Laboratory for XAS measurements at beamlines 12BM was supported by the U.S. Department of Energy under contract no. DE-AC02-06CH11357. M.G acknowledges the supports of the National Science Foundation of China (No. 12004156), and Shenzhen Basic Research Fund (JCYJ20190809181601639). The TEM work (M.G.) used the resources of the Pico Center from SUSTech Core Research Facilities that receive support from the Presidential Fund and Development and Reform Commission of Shenzhen Municipality. G.W. and B.L. acknowledge support from the US National Science Foundation (DMR 1905572). Computational resources were provided by the University of Pittsburgh Center for Research Computing as well as the Extreme Science and Engineering Discovery Environment, which is supported by National Science Foundation under grant no. ACI-1053575.

Conflict of interest

The authors declare no conflict of interest.

Author contributions

Y.Y. conceived the concept and led the project. W.Z. synthesized the materials and conducted the electrochemical measurements. W.Z., G.W., and Z.L. performed SEM, XPS, UPS, XRD, and Raman characterizations. Y.Z. and M.G. conducted the TEM characterization. W.Z. analyzed the TEM data under the direction of Y.Z. M.W., H.Z., and Z.F. performed the XAS measurements and analyses and wrote the corresponding XAS section. B. L. and G. W. performed DFT calculations.

W.Z. analyzed the data and wrote the manuscript. J.C. and Y.Y. oversaw all the results and revised the manuscript. All authors approved the manuscript.

Nomenclature:

SMSI	strong metal support interaction	FOS	functionally oxygenated supports
PGMs	platinum group metals	EDS	energy-dispersive X-ray spectroscopy
ORR	oxygen reduction reaction	OER	oxygen evolution reaction
PF	porous film	BE	binding energy
ZAFB	zinc-air flow batteries	ZAB	zinc-air batteries
XRD	X-ray diffraction	UPS	ultraviolet photoelectron spectroscopy
XPS	X-ray photoelectron spectroscopy	WF	work function
SEM	scanning electron microscopy	TEM	transmission electron microscopy
ECSA	electrochemically active surface area	XAS	X-ray absorption spectroscopy
OCP	open circuit potential	CV	cyclic voltammetry
RHE	reversible hydrogen electrode	LSV	linear sweep voltammetry
n	electron transfer number	$\chi_{\text{H}_2\text{O}_2}(\%)$	hydrogen peroxide yield
E_{onset}	onset potential	$E_{1/2}$	half-wave potential
J_{d}	diffusion-limiting current	SA	specific activity
MA	mass activity	EDLC	electrical double layer capacitance
RRDE	rotating ring disk electrode		
EXAFS	extended X-ray absorption fine structure		
XANES	X-ray absorption near edge structure		
EIS	electrochemical impedance spectroscopy		
HAADF-STEM	high-angle annular dark-field scanning transmission electron microscopy		

References

1. L. Trahey, F. R. Brushett, N. P. Balsara, G. Ceder, L. Cheng, Y.-M. Chiang, N. T. Hahn, B. J. Ingram, S. D. Minteer, J. S. Moore, K. T. Mueller, L. F. Nazar, K. A. Persson, D. J. Siegel, K. Xu, K. R. Zavadil, V. Srinivasan and G. W. Crabtree, *Proc. Natl. Acad. Sci.*, 2020, **117**, 12550.
2. Z. P. Cano, D. Banham, S. Ye, A. Hintennach, J. Lu, M. Fowler and Z. Chen, *Nat. Energy*, 2018, **3**, 279-289.
3. J. Fu, Z. P. Cano, M. G. Park, A. Yu, M. Fowler and Z. Chen, *Adv. Mater.*, 2017, **29**, 1604685.
4. J. Chang, G. Wang and Y. Yang, *Small Science*, 2021, **1**, 2100044.
5. J. Zhang, Z. Zhao, Z. Xia and L. Dai, *Nat. Nanotechnol.*, 2015, **10**, 444-452.
6. Y. Nie, L. Li and Z. Wei, *Chem. Soc. Rev.*, 2015, **44**, 2168-2201.
7. S. Ren, X. Duan, S. Liang, M. Zhang and H. Zheng, *J. Mater. Chem. A*, 2020, **8**, 6144-6182.
8. X. Wang, Z. Li, Y. Qu, T. Yuan, W. Wang, Y. Wu and Y. Li, *Chem*, 2019, **5**, 1486-1511.
9. M. Li, Z. Zhao, T. Cheng, A. Fortunelli, C.-Y. Chen, R. Yu, Q. Zhang, L. Gu, B. V. Merinov, Z. Lin, E. Zhu, T. Yu, Q. Jia, J. Guo, L. Zhang, W. A. Goddard, Y. Huang and X. Duan, *Science*, 2016, **354**, 1414.
10. C. Chen, Y. Kang, Z. Huo, Z. Zhu, W. Huang, H. L. Xin, J. D. Snyder, D. Li, J. A. Herron, M. Mavrikakis, M. Chi, K. L. More, Y. Li, N. M. Markovic, G. A. Somorjai, P. Yang and V. R. Stamenkovic, *Science*, 2014, **343**, 1339.
11. M. Luo, Z. Zhao, Y. Zhang, Y. Sun, Y. Xing, F. Lv, Y. Yang, X. Zhang, S. Hwang, Y. Qin, J.-Y. Ma, F. Lin, D. Su, G. Lu and S. Guo, *Nature*, 2019, **574**, 81-85.

12. G. Wang, J. Chang, S. Koul, A. Kushima and Y. Yang, *J. Am. Chem. Soc.*, 2021, **143**, 11595-11601.
13. W. Xia, A. Mahmood, Z. Liang, R. Zou and S. Guo, *Angew. Chem. Int. Ed.*, 2016, **55**, 2650-2676.
14. Y. Yang, M. Luo, W. Zhang, Y. Sun, X. Chen and S. Guo, *Chem*, 2018, **4**, 2054-2083.
15. M. Shao, Q. Chang, J.-P. Dodelet and R. Chenitz, *Chem. Rev.*, 2016, **116**, 3594-3657.
16. Y. Zhong, X. Xu, W. Wang and Z. Shao, *Batteries & Supercaps*, 2019, **2**, 272-289.
17. Q. Jia, S. Ghoshal, J. Li, W. Liang, G. Meng, H. Che, S. Zhang, Z.-F. Ma and S. Mukerjee, *J. Am. Chem. Soc.*, 2017, **139**, 7893-7903.
18. S. J. Tauster, S. C. Fung, R. T. K. Baker and J. A. Horsley, *Science*, 1981, **211**, 1121.
19. L. Zhang, L. Wang, C. M. B. Holt, T. Navessin, K. Malek, M. H. Eikerling and D. Mitlin, *The J. Phys. Chem. C*, 2010, **114**, 16463-16474.
20. Y. Lu, Y. Jiang, X. Gao, X. Wang and W. Chen, *J. Am. Chem. Soc.*, 2014, **136**, 11687-11697.
21. E. Antolini, J. R. C. Salgado and E. R. Gonzalez, *Journal of Power Sources*, 2006, **160**, 957-968.
22. W. Gao, Z. Zhang, M. Dou and F. Wang, *ACS Catal.*, 2019, **9**, 3278-3288.
23. Y. Liu and W. E. Mustain, *J. Am. Chem. Soc.*, 2013, **135**, 530-533.
24. Z.-F. Huang, J. Song, S. Dou, X. Li, J. Wang and X. Wang, *Matter*, 2019, **1**, 1494-1518.
25. S. J. Tauster, S. C. Fung and R. L. Garten, *J. Am. Chem. Soc.*, 1978, **100**, 170-175.
26. S. Shan, J. Li, Y. Maswadeh, C. O'Brien, H. Kareem, D. T. Tran, I. C. Lee, Z.-P. Wu, S. Wang, S. Yan, H. Cronk, D. Mott, L. Yang, J. Luo, V. Petkov and C.-J. Zhong, *Nat. Commun.*, 2020, **11**, 4201.

27. C. Jackson, G. T. Smith, D. W. Inwood, A. S. Leach, P. S. Whalley, M. Callisti, T. Polcar, A. E. Russell, P. Levecque and D. Kramer, *Nat. Commun.*, 2017, **8**, 15802.
28. H. Xu, H. Shang, C. Wang and Y. Du, *Small*, 2021, **17**, 2005092.
29. Y. Feng, Q. Shao, Y. Ji, X. Cui, Y. Li, X. Zhu and X. Huang, *Sci. Adv.*, 2018, **4**, eaap8817.
30. A. Chen and C. Ostrom, *Chem. Rev.*, 2015, **115**, 11999-12044.
31. W. Xiao, M. A. Liutheviene Cordeiro, M. Gong, L. Han, J. Wang, C. Bian, J. Zhu, H. L. Xin and D. Wang, *J. Mater. Chem. A*, 2017, **5**, 9867-9872.
32. K. Liang, L. Guo, K. Marcus, S. Zhang, Z. Yang, D. E. Perea, L. Zhou, Y. Du and Y. Yang, *ACS Catal.*, 2017, **7**, 8406-8412.
33. K. A. Stoerzinger, M. Risch, B. Han and Y. Shao-Horn, *ACS Catal.*, 2015, **5**, 6021-6031.
34. H.-S. Oh, H. N. Nong, T. Reier, A. Bergmann, M. Gliuch, J. Ferreira de Araújo, E. Willinger, R. Schlögl, D. Teschner and P. Strasser, *J. Am. Chem. Soc.*, 2016, **138**, 12552-12563.
35. X. Shen, T. Nagai, F. Yang, L. Q. Zhou, Y. Pan, L. Yao, D. Wu, Y.-S. Liu, J. Feng, J. Guo, H. Jia and Z. Peng, *J. Am. Chem. Soc.*, 2019, **141**, 9463-9467.
36. Q. Wang, X. Huang, Z. L. Zhao, M. Wang, B. Xiang, J. Li, Z. Feng, H. Xu and M. Gu, *J. Am. Chem. Soc.*, 2020, **142**, 7425-7433.
37. J. Yin, Y. Li, F. Lv, Q. Fan, Y.-Q. Zhao, Q. Zhang, W. Wang, F. Cheng, P. Xi and S. Guo, *ACS Nano*, 2017, **11**, 2275-2283.
38. C. C. L. McCrory, S. Jung, J. C. Peters and T. F. Jaramillo, *J. Am. Chem. Soc.*, 2013, **135**, 16977-16987.

39. A. Allagui, T. J. Freeborn, A. S. Elwakil and B. J. Maundy, *Scientific Reports*, 2016, **6**, 38568.
40. J. Lin, H. Jia, H. Liang, S. Chen, Y. Cai, J. Qi, C. Qu, J. Cao, W. Fei and J. Feng, *Adv. Sci.*, 2018, **5**, 1700687.
41. T.-J. Wang, F.-M. Li, H. Huang, S.-W. Yin, P. Chen, P.-J. Jin and Y. Chen, *Adv. Funct. Mater.*, 2020, **30**, 2000534.
42. H. Huang, J. Liu, P. Sun, S. Ye and B. Liu, *RSC Adv.*, 2017, **7**, 7406-7412.
43. D. Wang, Q. Li, C. Han, Q. Lu, Z. Xing and X. Yang, *Nat. Commun.*, 2019, **10**, 3899.
44. M. A. Peck and M. A. Langell, *Chem. Mater.*, 2012, **24**, 4483-4490.
45. O. Lupan, V. Postica, M. Hoppe, N. Wolff, O. Polonskyi, T. Pauporté, B. Viana, O. Majérus, L. Kienle, F. Faupel and R. Adelung, *Nanoscale*, 2018, **10**, 14107-14127.
46. S. Jayabal, G. Saranya, D. Geng, L.-Y. Lin and X. Meng, *J. Mater. Chem. A*, 2020, **8**, 9420-9446.
47. M. S. Ureta-Zañartu, C. Berriós, J. Pavez, J. Zagal, C. Gutiérrez and J. F. Marco, *J. Electroanal. Chem.*, 2003, **553**, 147-156.
48. F. Pan, Z. Li, Z. Yang, Q. Ma, M. Wang, H. Wang, M. Olszta, G. Wang, Z. Feng, Y. Du and Y. Yang, *Adv. Energy Mater.*, 2021, **11**, 2002204.
49. M. Sharma, J.-H. Jang, D. Y. Shin, J. A. Kwon, D.-H. Lim, D. Choi, H. Sung, J. Jang, S.-Y. Lee, K. Y. Lee, H.-Y. Park, N. Jung and S. J. Yoo, *Energy Environ. Sci.*, 2019, **12**, 2200-2211.
50. W. Liu, C. Lu, X. Wang, K. Liang and B. K. Tay, *J. Mater. Chem. A*, 2015, **3**, 624-633.
51. M. Wang, L. Árnadóttir, Z. J. Xu and Z. Feng, *Nanomicro Lett*, 2019, **11**, 47.

52. H. Liao, C. Wei, J. Wang, A. Fisher, T. Sritharan, Z. Feng and Z. J. Xu, *Adv. Energy Mater.*, 2017, **7**, 1701129.
53. R. Zhang, L. Wang, Y.-H. Ma, L. Pan, R. Gao, K. Li, X. Zhang and J.-J. Zou, *J. Mater. Chem. A*, 2019, **7**, 10010-10018.
54. C. Qiu, S. Wang, R. Gao, J. Qin, W. Li, X. Wang, Z. Zhai, D. Tian and Y. Song, *Mater. Today Energy*, 2020, **18**, 100557.
55. D. C. Nguyen, D. T. Tran, T. L. L. Doan, D. H. Kim, N. H. Kim and J. H. Lee, *Adv. Energy Mater.*, 2020, **10**, 1903289.
56. G. Wang, Z. Yang, Y. Du and Y. Yang, *Angew. Chem., Int. Ed.*, 2019, **58**, 15848-15854.
57. Z. Li, W. Niu, Z. Yang, N. Zaman, W. Samarakoon, M. Wang, A. Kara, M. Lucero, M. V. Vyas, H. Cao, H. Zhou, G. E. Sterbinsky, Z. Feng, Y. Du and Y. Yang, *Energy Environ. Sci.*, 2020, **13**, 884-895.
58. B. S. Yeo and A. T. Bell, *The J. Phys. Chem. C*, 2012, **116**, 8394-8400.
59. Y. Zhong, X. Xu, J.-P. Veder and Z. Shao, *iScience*, 2020, **23**, 100943.
60. Y. Zhong, X. Xu, P. Liu, R. Ran, S. P. Jiang, H. Wu and Z. Shao, *Adv. Energy Mater.*, 2020, **10**, 2002992.
61. X. Wang, J. Sunarso, Q. Lu, Z. Zhou, J. Dai, D. Guan, W. Zhou and Z. Shao, *Adv. Energy Mater.*, 2020, **10**, 1903271.
62. P. Wang, Y. Lin, L. Wan and B. Wang, *ACS Appl. Mater. Interfaces*, 2019, **11**, 37701-37707.
63. J. Qian, X. Bai, S. Xi, W. Xiao, D. Gao and J. Wang, *ACS Appl. Mater. Interfaces*, 2019, **11**, 30865-30871.

64. C. Zhu, Z. Yin, W. Lai, Y. Sun, L. Liu, X. Zhang, Y. Chen and S.-L. Chou, *Adv. Energy Mater.*, 2018, **8**, 1802327.
65. R. Zhao, Q. Li, Z. Chen, V. Jose, X. Jiang, G. Fu, J.-M. Lee and S. Huang, *Carbon*, 2020, **164**, 398-406.
66. P. Zhang, D. Bin, J.-S. Wei, X.-Q. Niu, X.-B. Chen, Y.-Y. Xia and H.-M. Xiong, *ACS Appl. Mater. Interfaces*, 2019, **11**, 14085-14094.
67. Y. Cheng, Y. Wang, Q. Wang, Z. Liao, N. Zhang, Y. Guo and Z. Xiang, *J. Mater. Chem. A*, 2019, **7**, 9831-9836.
68. F. Kong, X. Fan, A. Kong, Z. Zhou, X. Zhang and Y. Shan, *Adv. Func. Mater.*, 2018, **28**, 1803973.
69. G. Fu, Y. Liu, Y. Chen, Y. Tang, J. B. Goodenough and J.-M. Lee, *Nanoscale*, 2018, **10**, 19937-19944.
70. D. Bin, B. Yang, C. Li, Y. Liu, X. Zhang, Y. Wang and Y. Xia, *ACS Appl. Mater. Interfaces*, 2018, **10**, 26178-26187.
71. Y. Cheng, Y. Guo, N. Zhang, S. Tao, Z. Liao, Y. Wang and Z. Xiang, *Nano Energy*, 2019, **63**, 103897.
72. J. Han, X. Meng, L. Lu, J. Bian, Z. Li and C. Sun, *Adv. Func. Mater.*, 2019, **29**, 1808872.

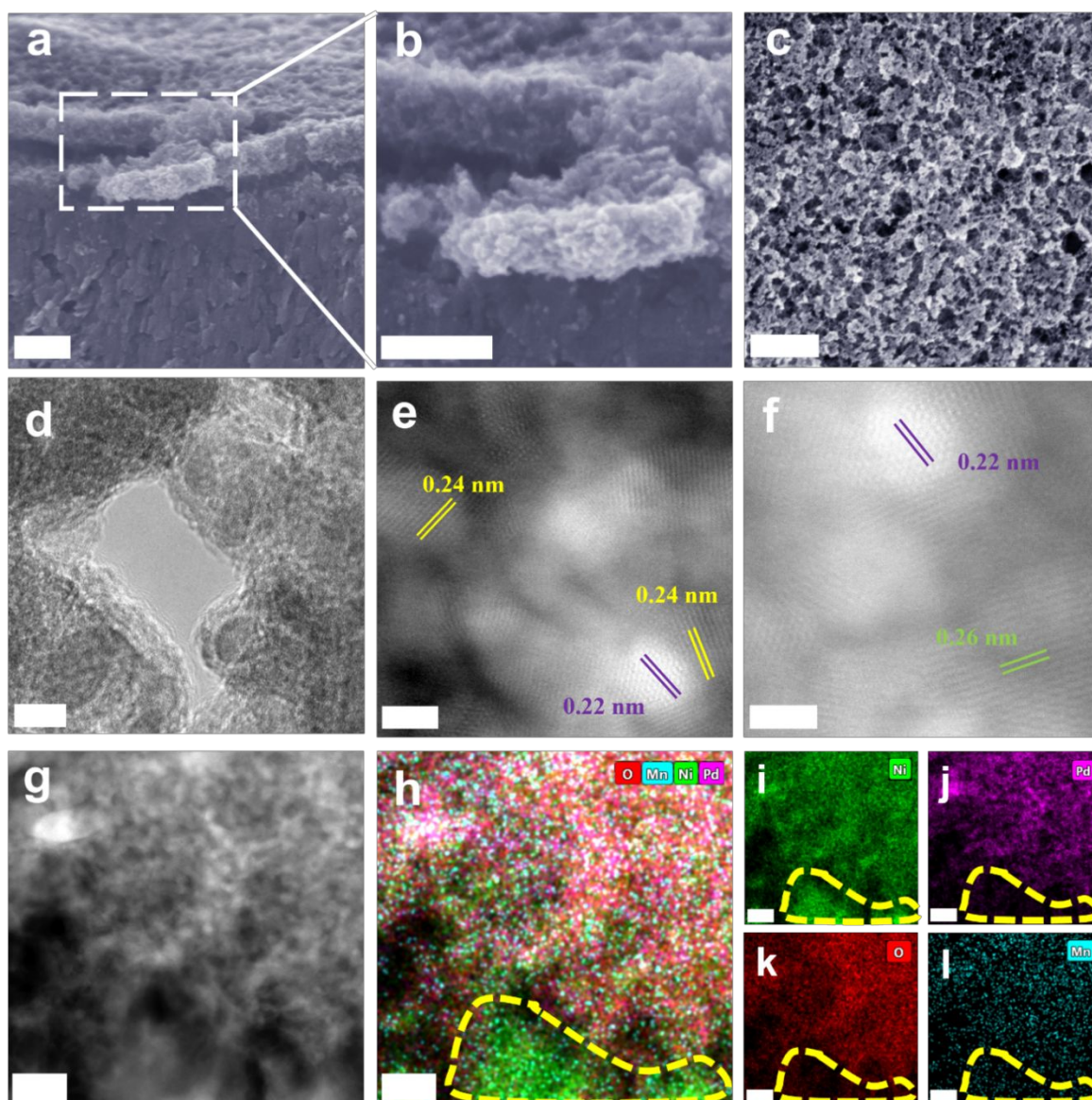


Figure 1. Microscopic characterizations of PdNiMnO-PF. (a-c) Cross-sectional, enlarged, and top-view SEM images, respectively. (d) HRTEM and (e-f) STEM-HAADF images. Lattice fringes of Pd, PdO, and NiO are marked with purple, green, and yellow colors, respectively. (g) HAADF image and (h-l) corresponding EDS mappings. Scale bars: (a-c) 200 nm, (d) 5 nm, (e-f) 2 nm, and (g-i) 20 nm.

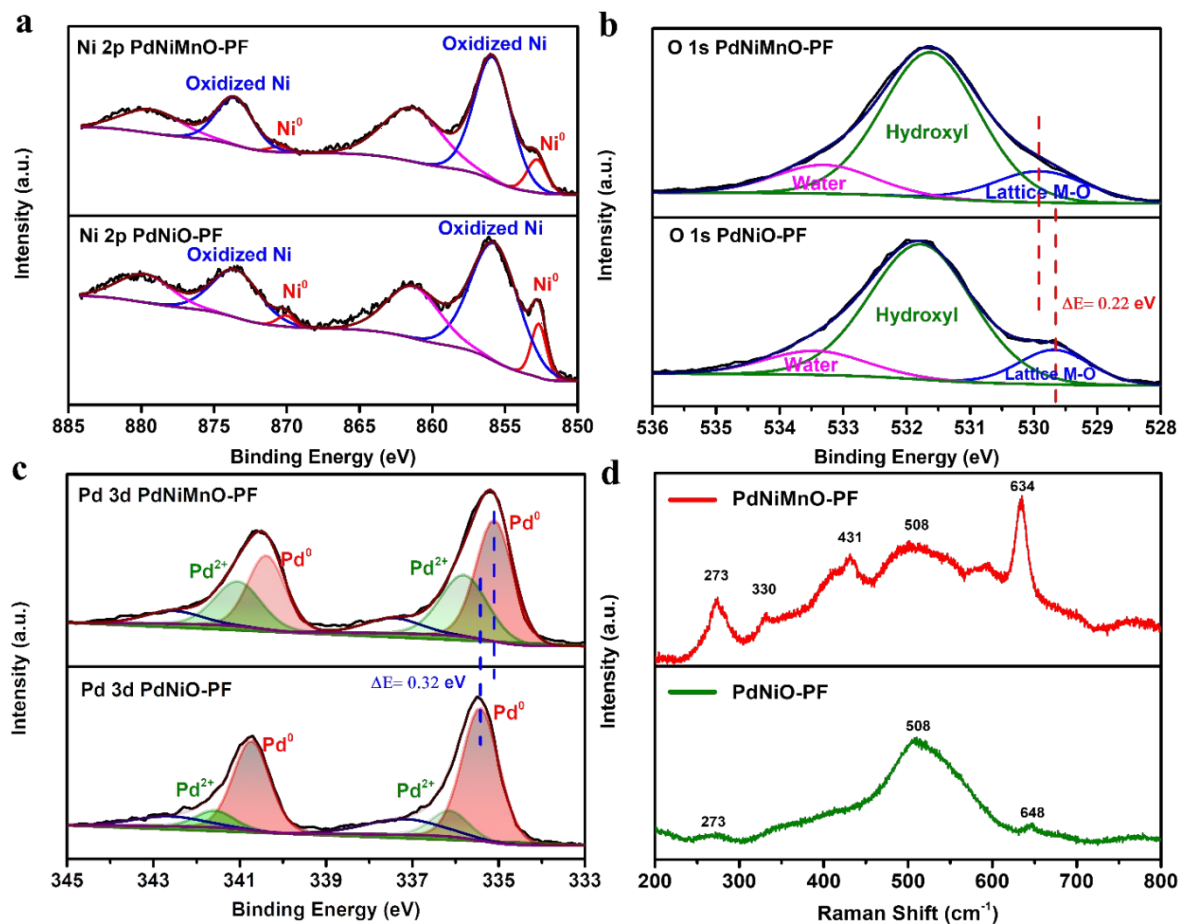


Figure 2. Spectroscopic characterizations of PdNiMnO-PF. High-resolution XPS spectra of (a) Ni 2p, (b) O 1s and (c) Pd 3d for PdNiMnO-PF (top) and PdNiO-PF (bottom). (d) Raman spectra of PdNiMnO-PF (top) and PdNiO-PF (bottom).

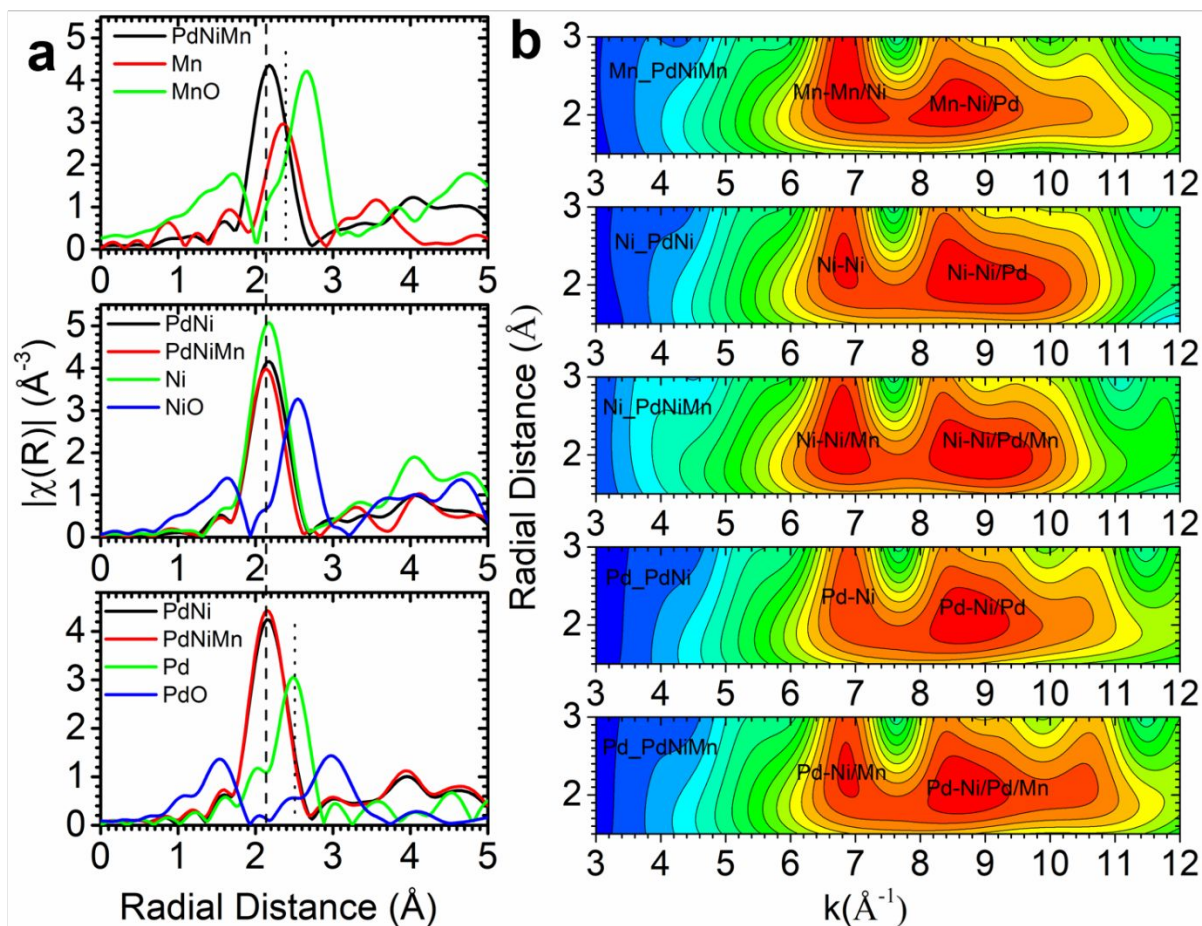


Figure 3. XAS characterizations. (a) Fourier Transform R-space of Mn K-edge, Ni K-edge, and Pd K-edge (from top to bottom), the dash indicates Mn-Ni/Mn, Ni-Mn/Ni/Pd, and Pd-Mn/Ni/Pd bonds, the dotted line indicates Mn-Mn and Pd-Pd bonds. (b) Wavelet Transform of Mn K-edge for PdNiMn, Ni K-edge for PdNi, Ni K-edge for PdNiMn, Pd K-edge for PdNi, and Pd K-edge for PdNiMn (from top to bottom).

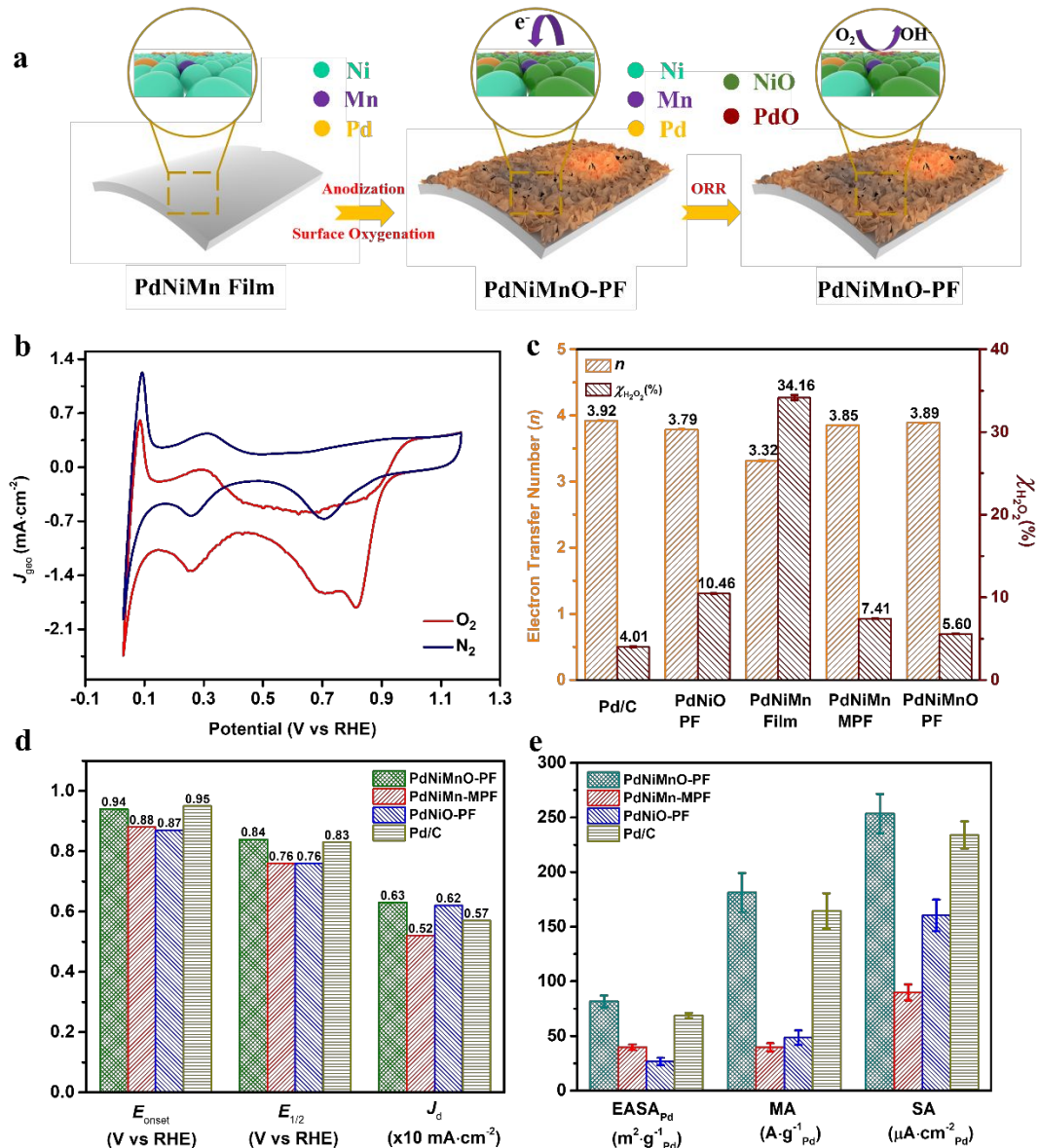


Figure 4. Electrochemical Performance. (a) Schematic illustration of surface oxygenation and working principle of PdNiMnO-PF catalyst during ORR. (b) Cyclic voltammetry (CV) curves of PdNiMnO-PF performed in O₂- and N₂-saturated electrolytes. (c) Comparison of electron transfer number (*n*) and hydrogen peroxide yield ($\chi_{\text{H}_2\text{O}_2}$ (%)) for Pd/C, PdNiO-PF, PdNiMn film, PdNiMn-MPF and PdNiMnO-PF under 0.4 V (V VS RHE). (d) Comparison of E_{onset} , $E_{1/2}$, and J_d for PdNiMnO-PF, PdNiMn-MPF, PdNiO-PF, and Pd/C. (e) Comparison of EASApd, MA, and SA for PdNiMnO-PF, PdNiMn-MPF, PdNiO-PF, and Pd/C.

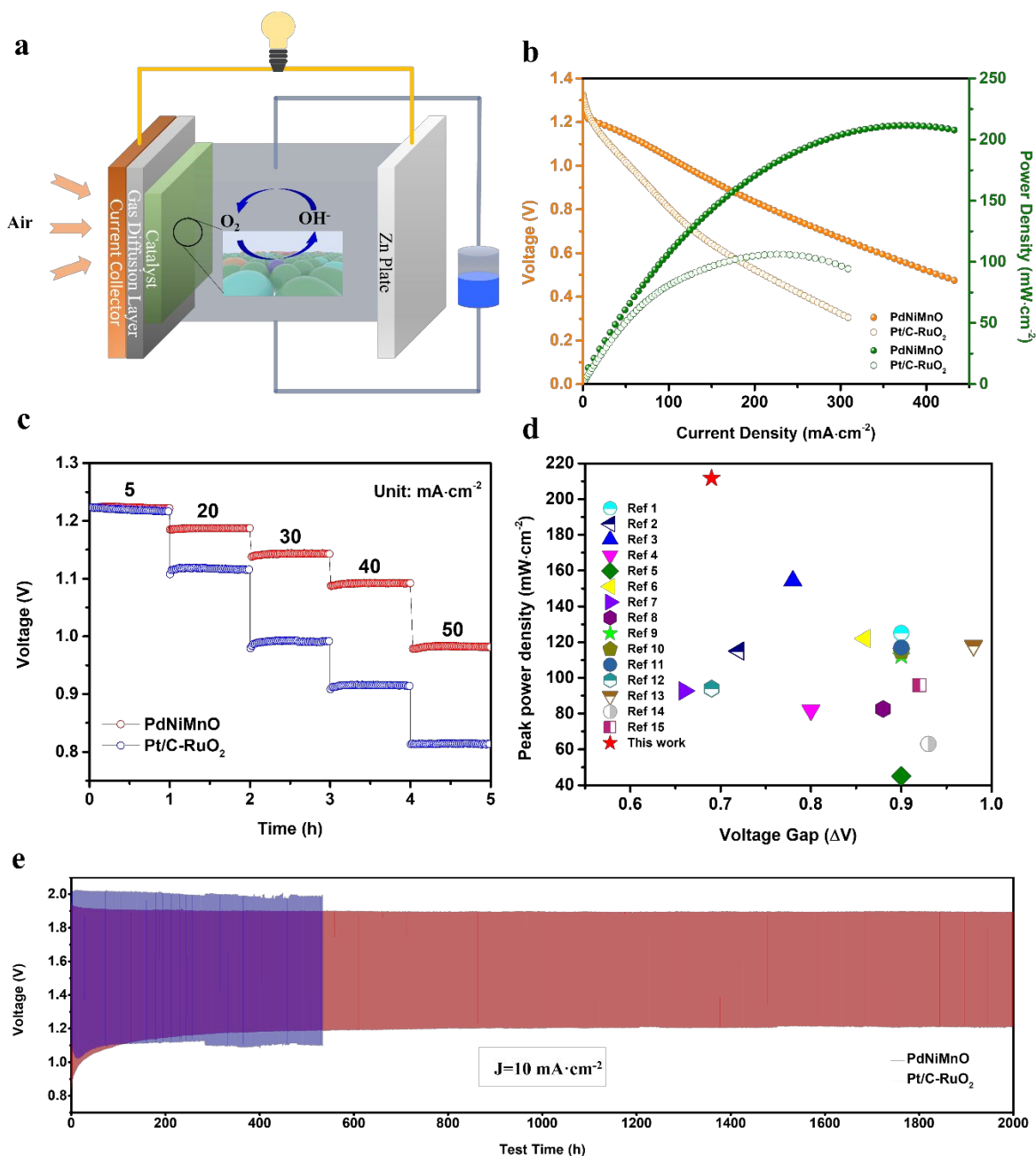


Figure 5. ZAFB performance. (a) Schematic illustration of working principle of an aqueous zinc-air flow battery. (b) Comparison of polarization and power density curves for PdNiMnO and Pt/C-RuO₂. (c) Comparison of discharging behavior of PdNiMnO and Pt/C-RuO₂ based ZAFBs at various current densities. (d) A characteristic plot of peak power density vs voltage gap for this work and other references. (e) Long-term Galvanostatic discharge-charge cycling stability of ZAFB (PdNiMnO) at a current density of 10 mA·cm⁻².